Scattering of waves in locally resonant woodpile structures with impurities

Yeongtae Jang,[1,2] Eunho Kim,[3,4,5,*] and Junsuk Rho[1,6,7,8,†]

[1]Department of Mechanical Engineering, Pohang University of Science and Technology (POSTECH), Pohang 37673, Republic of Korea
[2]Department of Mechanical Engineering, Kangwon National University, Samcheok 25913, Republic of Korea
[3]Division of Mechanical System Engineering, Jeonbuk National University, Jeonju 54896, Republic of Korea
[4]Department of JBNU-KIST Industry-Academia Convergence Research, Jeonju 54896, Republic of Korea
[5]Graduate School of Mechanical-Aerospace-Electric Convergence Engineering, Jeonbuk National University, Jeonju 54896, Republic of Korea
[6]Department of Chemical Engineering, Pohang University of Science and Technology (POSTECH), Pohang 37673, Republic of Korea
[7]Department of Electrical Engineering, Pohang University of Science and Technology (POSTECH), Pohang 37673, Republic of Korea
[8]POSCO-POSTECH-RIST Convergence Research Center for Flat Optics and Metaphotonics, Pohang 37673, Korea

(Received 24 May 2026; accepted 30 June 2026; published 4 September 2026)

We theoretically and experimentally investigate wave scattering in a single-column woodpile structure with impurities. This structure consists of slender cylindrical beams that support flexural bending modes, which are coupled strongly with propagating waves in the low-frequency regime (i.e., local resonance coupling). We examine the linear scattering of plane waves from single and double impurities in periodic configurations. When local resonance coupling is neglected, the double-impurity configuration exhibits reflectionless transmission, resembling the Ramsauer-Townsend (RT) resonance. Further analysis reveals that, under strong local resonance coupling, this behavior evolves into a Fano resonance, which features an asymmetric line shape with a sharp transition between transmission and reflection. However, as the RT resonance and the local resonance become spectrally closer, an analog of electromagnetically induced transparency (EIT) emerges, resulting from the balanced interference between the two modes. These distinct resonant behaviors can be tuned by varying the local resonance coupling strength, providing a controllable platform for macroscopic analogs of quantum wave interference. Potential applications include vibration isolation and wave-based switching devices.

DOI: 10.1103/rwtw-8tvm

I. INTRODUCTION

A woodpile structure—a type of granular crystal—consists of a regularly arranged assembly of discrete particles that interact through elastic collisions. A key feature of such discrete systems is the inherent nonlinearity arising from contact interactions and the discrete nature of the medium, enabling the exploration of diverse wave dynamics [1–3]. One particularly attractive aspect is their highly tunable dynamic response, which can be adjusted via an applied static load. This tunability allows for investigations across nearly linear, weakly nonlinear, and strongly nonlinear regimes [4–6]. The ability to control stress wave propagation in these architectures has been widely demonstrated [6], supporting applications such as filtering [7,8], shock absorption [9–11], acoustic diodes [12,13], logic gates [14], and nondestructive evaluation [15].

Among various geometries of unit granules (e.g., spherical, toroidal, and elliptical shapes [3]), woodpile structures are composed of slender cylindrical beams that support flexural vibrations. These bending modes induce local resonance effects when coupled with propagating waves, leading to richer wave dynamics [16–22]. Despite these advantages, the investigation of diverse wave dynamics in such systems has been limited due to the constraints of theoretical models. Recent advances in physics-informed discrete element modeling [23] have overcome these limitations, enabling more comprehensive exploration of wave behaviors, especially in structurally complex systems such as those with inhomogeneities.

Inhomogeneous configurations, in particular, give rise to intriguing wave dynamics. For example, even in traditional granular crystals without local resonance coupling, inhomogeneity can give rise to classical analogs of quantum phenomena, such as the Ramsauer-Townsend (RT) effect [24]. This effect, originally observed as a sharp minimum in the electron scattering cross-section at low energies for rare gas atoms, can be replicated in classical media, bringing quantum concepts [25] into the realm of classical mechanics. Indeed, a wide range of wave phenomena at the atomic and quantum levels—such as strong coupling [26], electromagnetically induced transparency (EIT) [27], level repulsion [28], and both adiabatic and nonadiabatic processes [29]—can be effectively described using coupled harmonic oscillators. In addition, macroscopic experiments have successfully demonstrated analogs of phenomena such as Landau-Zener tunneling [30,31] and Anderson localization [32,33], and others [34,35]. These studies collectively show that exploring wave dynamics in macroscopic classical systems provides intuitive insights into atomic- and quantum-scale phenomena, owing to their analogous wave physics [36].

*Contact author: eunhokim@jbnu.ac.kr
†Contact author: jrsho@postech.ac.kr

In this work, we investigate linear wave scattering in a single-column woodpile structure with embedded impurities. Our key finding is that a classical analog of the RT resonance transitions into a Fano resonance through coupling with local resonance, especially in the case of a double-impurity chain. Fano resonance is characterized by a sharp transition in the transmission-reflection spectrum, where total transmission abruptly shifts to reflection. Traditionally, Fano resonances arise from the interference between a discrete quantum state and a continuum of states [37]. Analogously, in our system, the discrete local resonance mode induced by impurities interferes with the continuum band that supports the RT resonance, resulting in an asymmetric line shape. Furthermore, we demonstrate that as the RT resonance and the local resonance become spectrally closer, a mechanical analog of the EIT phenomenon emerges [38]. This work highlights that a series of resonance phenomena—RT, Fano, and EIT-like—can be systematically accessed within a single mechanical system by controlling the impurity-induced local resonance coupling. These tunable and distinctive wave behaviors in a mechanical platform offer promising potential for applications in switching devices, sensing, and wave control technologies.

This paper is structured as follows: In Sec. II, we introduce the model setup and describe the discrete element model and corresponding band structures of the woodpile structure. In Sec. III, we discuss our analytical, numerical, and experimental approaches to the linear scattering problem involving single and double impurities embedded in homogeneous woodpile structures. In Sec. IV, we discuss and compare the results from theory, computations, and experiments. We demonstrate that RT resonance in our system transitions into a Fano resonance through coupling with local resonance. In Sec. V, we present further simulations that show the emergence of multiple Fano resonances and the mechanical analog of EIT. Finally, Section VI concludes the paper and suggests potential avenues for future research.

II. WOODPILE STRUCTURES

Figures 1(a) and 1(b) show the woodpile lattices with single and double impurities, consisting of slender cylindrical beams whose centers form orthogonal contacts with neighboring elements. The host cylinder (i.e., background medium) has a length L_h, while the defect cylinder has a length L_p, both with identical radii. By varying L_p and keeping L_h fixed, we investigate wave scattering arising from the interaction between plane waves and local resonance. Thus, changes in cylinder length affect the bending vibration frequency and, in turn, the local resonance coupling. Accordingly, we define the length ratio as $\Lambda = L_h/L_p$. The elastic potential between the cylinders is derived from nonlinear Hertz contact [39]. Under sufficiently strong static precompression within this lattice, as is the case here, the response to small external perturbations can be described by linear dynamics.

We analyze the system dynamics using a discrete element model. In this approach, we represent the "continuum" cylinder as "discretized" mass-with-mass unit cells [see Fig. 1(c)], with contacts modeled as springs following the linearized contact stiffness β_r (see Appendix A for details). The local resonance coupling arising from the cylinder's bending

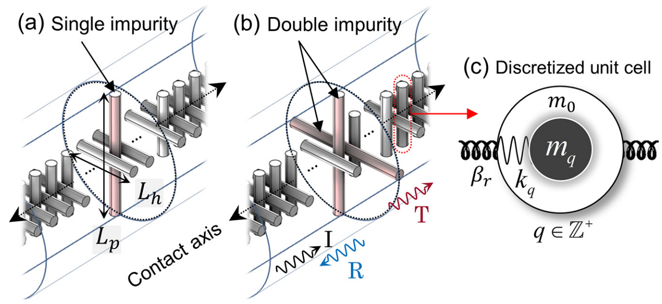

FIG. 1. Schematic of one-dimensional woodpile structures with (a) a single impurity and (b) double impurities, composed of slender cylindrical beams. Each beam contacts neighboring beams orthogonally through their centers of mass. The length of the host beam is denoted as L_h, while the length of the impurity beam is L_p. An incident plane wave (I) leads to reflected (R) and transmitted (T) waves upon interaction with the impurity. (c) A theoretical discretized unit cell that describes the dynamics of a single continuous beam. The internal harmonic oscillator, represented by local mass m_q and spring constant k_q, captures the wave physics of local resonance effects.

vibration modes is modeled as multiple harmonic oscillators (m_q and k_q, where q denotes the mode number) within these discrete unit cells. The mechanical coefficients of the multiple harmonic oscillators (e.g., m_0, m_q, and k_q $\forall q \in [1, \infty]$) are determined via physics-informed discrete element modeling, as established in the author's previous work [23]. This method establishes a correspondence between the wave physics described by continuum beam theory and that captured by the discrete model, ensuring that the discretized unit cell faithfully represents the effects of local resonance coupling. As a result, this framework allows for the analytical mapping of cylindrical elements—with varying geometries and material properties—into discrete unit cells that accurately capture their local resonance behavior and associated wave dynamics. For simplicity, detailed mathematical derivations are omitted in the main text; however, we summarize the equivalent masses and spring constants associated with multiple bending modes as a function of cylinder length in Appendix B.

A. Band structures

We first investigate the dynamics of a pure homogeneous chain without impurities. This can be achieved by examining the band structure derived from the dispersion relationship. In the context of an infinite chain configuration, the equations of motion for the nth unit cell are

$$m_{n,0}\ddot{u}_n = \beta_r(u_{n-1} - 2u_n + u_{n+1}) + \sum_q k_{n,q}(u_{n,q} - u_n), \quad (1)$$

$$m_{n,q}\ddot{u}_{n,q} = k_{n,q}(u_n - v_{n,q}), \quad \forall q \in \mathbb{Z}^+, \quad (2)$$

where u_n and $u_{n,q}$ represent the displacements of masses $m_{n,0}$ and $m_{n,q}$, respectively; q is the mode number. Under the harmonic oscillations of these masses, i.e., $u_n = \boldsymbol{U}\exp(i\omega t)$ and $u_{n,q} = \boldsymbol{U}_q\exp(i\omega t)$, we can obtain the following relation from Eq. (2):

$$u_{n,q} = \frac{\omega_q^2}{\omega_q^2 - \omega^2}u_n, \quad \forall q \in \mathbb{Z}^+. \quad (3)$$

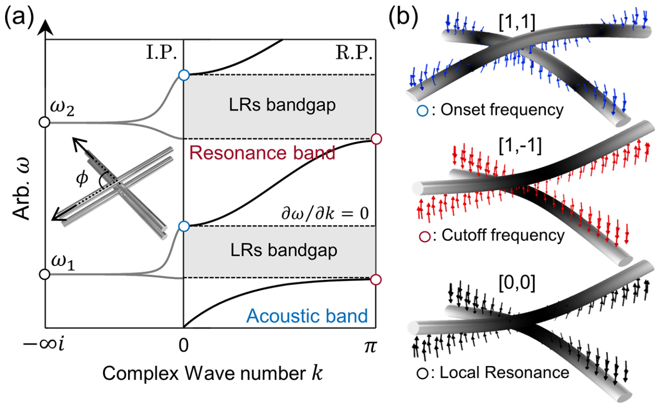

FIG. 2. (a) Schematic of the band structures for homogeneous woodpile structures as a function of the complex wave number. The right-hand side shows the real part (R.P.) of the wave number, while the left-hand side shows the imaginary part (I.P.). The branches are categorized into the acoustic band (first branch) and upper resonance bands, which arise from multiple local resonance modes. The gray region indicates the local resonance bandgap. (b) Vibrational bending modes of the cylindrical beams at the boundary of the Brillouin zone, correspond to the circled frequencies in the band structures shown in panel (a). These modes are characterized by zero group velocity.

Here, $\omega_q = \sqrt{k_q/m_q}$ denotes the resonant frequency of the multiple harmonic oscillator. By substituting this relation into Eq. (1), one can obtain

$$-m_{\text{eff}}(\omega)\omega^2 u_n = \beta_r(u_{n-1} - 2u_n + u_{n+1}), \tag{4}$$

where

$$m_{\text{eff}}(\omega) = m_0 + \sum_q m_q \frac{\omega_q^2}{\omega_q^2 - \omega^2}. \tag{5}$$

Explicitly, Eq. (4) represents the harmonic wave solution of a well-known monatomic chain, but with an effective mass m_{eff}. By applying Floquet's theorem [40], i.e., $u_{n\pm1} = u_n \exp(\mp ik)$, one can derive the dispersion relation for locally resonant systems,

$$m_{\text{eff}}\omega^2 = 4\beta_r \sin^2 \frac{k}{2}, \tag{6}$$

where k is the wave number. This relationship yields the band structure as a function of the complex wave number, as shown in Fig. 2(a). The real part (R.P.) of the wave number is shown on the right, while the imaginary part (I.P.) is displayed on the left. We observe multiple branches resulting from the coupling of various local resonances, with local resonance bandgaps (gray area) appearing between these branches. The branches are classified into two types: the *acoustic bands*, which are primarily governed by the rigid-body motions of the cylinders without local vibration modes, and the *resonance bands*, which resemble the acoustic bands in terms of wave propagation through the chain, but are distinguished by the presence of local resonance modes within the individual cylinders. All branches are formed at different frequencies but share the same wave-number range, which arises from the Brillouin zone of the periodic chain. As previously noted, increasing the length of the cylinder causes each branch to shift to lower frequencies, in accordance with the relation $\omega \propto L^{-2}$ of the bending vibration modes [41].

We now briefly discuss the physical vibrational behavior associated with the band structure. In Fig. 2(b), we show the physical vibrational behavior of the cylindrical beam at the edge frequency of the first resonance bands and the local resonance frequency (black circle) within the bandgap. The frequency at which the resonance band initiates is the onset frequency (blue circle), while the frequency at which it terminates is the cutoff frequency (red circle). The arrows represent the displacement fields associated with the bending modes. Within a single branch, the onset, cutoff, and local resonance modes are all associated with the same bending mode. For example, the second branch reflects the characteristics of the first bending mode of the cylinder, as shown in Fig. 2(b). However, due to their distinct wave-number characteristics, the relative motion between the cylinders can be clearly distinguished.

For the onset frequency, where the wave number $k = 0$ corresponds to an infinite wavelength, the relative motion at the contact point between adjacent cylinders is in-phase—represented by the displacement vector [1,1]. In contrast, at the cutoff frequency, the smallest wavelength related to the lattice constant results in an out-of-phase motion at the contact point between cylinders, i.e., [1, −1]. These features result in a zero group velocity ($\partial\omega/\partial k = 0$) at both the onset and cutoff frequencies, corresponding to standing waves. The local resonance frequency, associated with an infinite imaginary wave number ($k = -i\infty$), corresponds to a stationary state—i.e., [0,0]—in which both cylinders remain motionless at the contact point due to vibration isolation [23].

Through this band structure configuration, we can consider two types of wave-scattering scenarios: (1) local resonance coupling of impurities in the rigid-dominant acoustic band of the host chain and (2) local resonance coupling of impurities in the resonance band of the host chain. We analyze the scattering problem in both scenarios.

III. SCATTERING OF WAVES BY IMPURITIES

Building on the impurity formations illustrated in Figs. 1(a) and 1(b), we now focus on the scattering of harmonic waves by these impurities in the system. To simplify the theoretical analysis, we reformulate the equation of motion Eq. (1) by focusing on the response u_n of the primary mass (m_0).

$$m_{n,0}\ddot{u}_n = \beta_r(u_{n-1} - 2u_n + u_{n+1}) + \sum_q k_{n,q}\Delta_{n,q}u_n, \tag{7}$$

where

$$\Delta_{n,q} = \frac{\omega^2}{\omega_{n,q}^2 - \omega^2}, \quad \forall q \in \mathbb{Z}^+. \tag{8}$$

We note that, even with the introduction of impurities, the linearized contact stiffness of the spring (β_r) remains constant due to the identical contact angle between cylinders, as the defect cylinders modify only their length.

A. Analytic approach

To explore the effect of impurities on the scattering problem, we utilize the following ansatz [37]:

$$u_n = \begin{cases} e^{i(kn-\omega t)} + Re^{-i(kn+\omega t)}, & \text{if } n \leqslant 0, \\ Te^{i(kn-\omega t)}, & \text{if } n > 0, \end{cases} \tag{9}$$

which models an incident plane wave producing reflected (R) and transmitted (T) waves upon interaction with the impurity ($n = 0$). From this interaction, we thereby define the reflection coefficient $|R|^2$ and transmission coefficient $|T|^2$. We note that, for a conservative system, the frequency of the incident plane waves remains unchanged when interacting with an impurity. However, a minor phase shift caused by the impurities may influence the wave number. Despite this, the wave number of both the incoming and outgoing waves in free space remains unchanged due to the energy-conserving nature of the system. Substituting Eq. (9) into the equation of motion near the single impurity yields a linear system of equations:

$$\mathcal{S}\begin{pmatrix} T \\ R \end{pmatrix} = \mathcal{D}, \tag{10}$$

where

$$\mathcal{S} = \begin{pmatrix} \beta_c e^{ik} & \widetilde{m}_0\omega^2 + \beta_c(e^{ik}-2) + \sum_q \widetilde{k}_q\widetilde{\Delta}_q \\ m_0\omega^2 e^{ik} + \beta_c e^{ik}(e^{ik}-2) + \sum_q k_q\Delta_q e^{ik} & \beta_c \end{pmatrix}, \tag{11}$$

$$\mathcal{D} = \begin{pmatrix} -\widetilde{m}_0\omega^2 + \beta_c(2-e^{-ik}) - \sum_q \widetilde{k}_q\widetilde{\Delta}_q \\ -\beta_r \end{pmatrix}. \tag{12}$$

For the mechanical properties associated with impurity cylinders, we use a tilde notation to indicate impurity-related parameters (i.e., $\widetilde{m}_0, \widetilde{k}_q$, and $\widetilde{\Delta}_q$). From the solution of Eq. (10), we can determine the reflection and transmission coefficients for the case of a single impurity. Analogously, in the case of a system with two impurities, we apply the following ansatz:

$$u_n = \begin{cases} e^{i(kn-\omega t)} + Re^{-i(kn+\omega t)}, & \text{if } n < -1, \\ T_0e^{i(k_\delta n-\omega t)} + R_0e^{-i(k_\delta n+\omega t)}, & \text{if } n = -1, 0, \\ Te^{i(kn-\omega t)}, & \text{if } n \geqslant 1, \end{cases} \tag{13}$$

where T_0 and R_0 indicate the reflected and transmitted waves generated between the two impurities ($n = -1, 0$); the k_δ is defined as $k + \delta$, where δ represents the difference between the wave numbers in the host chain and the impurity region. In this way, we can construct a linear system of equations for the double impurity case (see Appendix C for details).

In Figs. 3(a) and 3(b), the transmission and reflection coefficients of the acoustic band are shown as functions of k and Λ. The results reveal complementary behavior, where a reduction in one coefficient corresponds to an increase in the other, and vice versa. For single impurities, the reflection coefficient vanishes at $k = 0$ or $\Lambda = 1$ (indicated by gray dotted lines), corresponding to the long-wavelength regimes and homogeneous systems, respectively. Additionally, near $\Lambda \approx 3$, the reflection coefficient nearly vanishes over most values of k, because the passband associated with the impurity cylinder spectrally overlaps with the acoustic band of the fixed host-cylinder chain. However, at small wave numbers near $\Lambda \approx 3$, a transmissionless mode emerges because the impurity's local resonance frequency overlaps with the low-frequency region of the host acoustic band. This transmissionless mode follows the red arrow indicated in Fig. 3(b). In addition, this local resonance asymptotically approaches $k = 0$ as Λ increases, due to its growing influence on the host chain's acoustic band at low frequencies.

In Figs. 3(c) and 3(d), we present the coefficients for the first resonance band. In the resonance band, we observe that the reflection coefficient vanishes near several values of Λ, similar to the acoustic band. However, unlike the acoustic band, we distinctly observe a transmissionless mode at $k = 0$. This arises from the standing wave nature at $k = 0$ in the resonance branch of the host chain, where no energy is transferred within the chain——i.e., the group velocity is zero at $k = 0$ in the dispersion curve. Additionally, another difference from the acoustic band is the absence of coupling effects from the impurity's local resonance. This is because the local resonances of the host and impurity cylinders do not interact

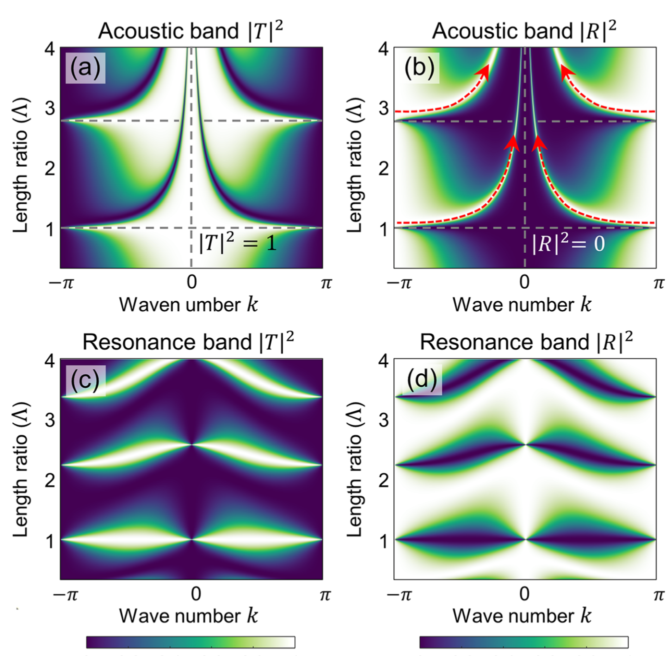

FIG. 3. (Left) Transmission and (right) reflection coefficients for the scattering of a plane wave in a woodpile chain with a single impurity, as functions of wave number k and length ratio Λ. The top panels correspond to the acoustic band, while the bottom panels represent the resonance band. In panel (b), the red arrows indicate the local resonance effect induced by the vibrational modes of the cylindrical beam.

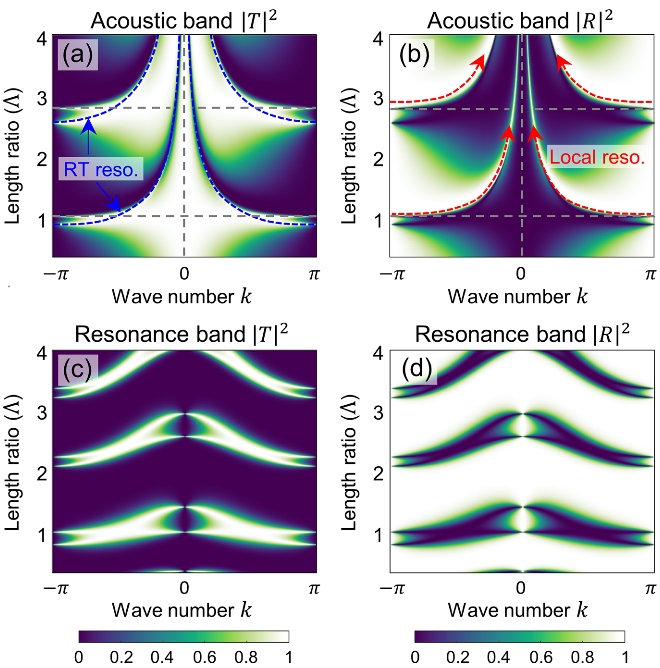

FIG. 4. (Left) Transmission and (right) reflection coefficients for the scattering of a plane wave in a woodpile chain with double impurities. The blue dashed line in panel (a) highlights a special reflectionless mode at a specific wave number, representing the mechanical analog of the Ramsauer-Townsend (RT) resonance. This reflectionless mode also appears in the resonance band.

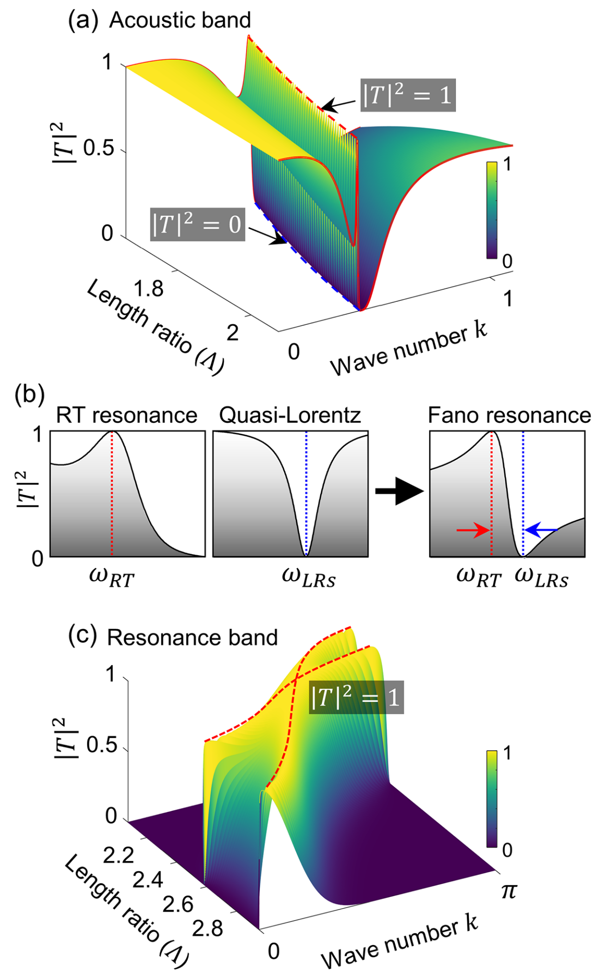

FIG. 5. Extracted transmission coefficient $|T|^2$ of the acoustic band for specific Λ and k ranges in Fig. 4(a). The red and blue dashed lines indicate where $|T|^2$ equals 1 and 0, respectively, and the red solid line represents the Fano resonance profile. (b) Schematic of Fano resonance formation in our system. This asymmetric Fano profile arises from the superposition of RT resonance induced by double impurities and local resonance induced by mode coupling. (c) Extracted transmission coefficient $|T|^2$ of the resonance band for specific Λ and k ranges in Fig. 4(c).

and are physically decoupled. At the discrete element level, this means that there is no coupling between the harmonic oscillators associated with the host cylinder and those of the impurity.

For the case of double impurities, Figs. 4(a) and 4(b) depict the transmission and reflection coefficients of the acoustic band, while Figs. 4(c) and 4(d) correspond to the resonance band. What is particularly interesting here is that, in addition to the trivial full-transmission conditions at $k = 0$ and $\Lambda = 1$, the double-impurity chain exhibits an additional full-transmission line at a finite wave number, $k = k_r \neq 0$, as indicated by the blue dotted line in Fig. 4(a). This phenomenon is the mechanical analog of the RT effect in quantum mechanics [25], which has been previously studied in granular crystals [24] and bistable chains [42]. At this special resonance mode, a wave passes completely through the impurities without scattering, experiencing only a phase shift.

Furthermore, our system presents two key aspects that are particularly noteworthy compared to previous studies. (i) When the local resonance effect of the impurity is considered, multiple RT-like resonances can appear, as indicated by the blue dotted line in Fig. 4(a). (ii) For $\Lambda > 1$, as Λ increases, the transmissionless mode driven by the impurity-induced local resonance [marked by the red arrow in Fig. 4(b)] approaches the RT-like full-transmission branch [marked by the blue dotted line in Fig. 4(a)]. This spectral proximity leads to a sharp transition between transmission and reflection, which is more clearly demonstrated by the extracted transmission profiles in Fig. 5.

To examine this sharp transition in more detail, we extracted $|T|^2$ from specific sections for selected Λ and k ranges, as shown in Fig. 5(a). In the acoustic band, we clearly observe asymmetric $|T|^2$ profiles with a sharp shift from total transmission to reflection. This asymmetric profile is a hallmark of the Fano resonance, typically understood in quantum mechanics as arising when a discrete quantum state interferes with a continuum of states [37]. Similarly, the woodpile lattice exhibits a Fano resonance analog, where the discrete local resonance state induced by impurities interferes with the continuum band supporting the RT resonance, resulting in an asymmetric line profile, as depicted in Fig. 5(b). Additionally, an interesting feature is that the resonance band supports RT resonance due to the presence of the double impurity, as shown in Fig. 5(c). However, because there is no local resonance coupling between the host and impurity cylinders, this RT resonance does not evolve into the asymmetric line shape characteristic of a Fano resonance.

Now, our key questions are: How can we mathematically derive these reflectionless modes that appear at $k = k_r$, how can the degree of asymmetric slope in the Fano resonance be determined? To answer this, we begin with a system made up of a simple lumped mass model without local resonance, which only supports the acoustic band. This can be achieved by increasing the local stiffness of the harmonic oscillators in the system to infinity (i.e., no vibration). For a system with double impurities, the reflection and transmission coefficients are given as follows:

$$|R|^2 = \left|\frac{e^{-2ik}(e^{ik}-1)(\rho-1)[2e^{ik}+\rho(1-2e^{ik}+e^{2ik})]}{(-3\rho^2+4\rho)e^{ik}+(3\rho^2-6\rho+3)e^{2ik}-(\rho^2-2\rho+1)e^{3ik}+\rho^2}\right|^2, \tag{14}$$

$$|T|^2 = \left|\frac{e^{ik}+1}{(-3\rho^2+4\rho)e^{ik}+(3\rho^2-6\rho+3)e^{2ik}-(\rho^2-2\rho+1)e^{3ik}+\rho^2}\right|^2, \tag{15}$$

where ρ is the ratio of the host lumped mass to the impurity lumped mass. Therefore, the transmission coefficients of the acoustic band obtained from these results are presented in the Appendix D. The reflectionless mode can be identified by setting $|R|^2 = 0$ in Eq. (14), resulting in the following expression:

$$k_r = \arccos\left(1 - \frac{1}{\rho}\right). \tag{16}$$

We note that these results are very similar to those in Ref. [42]. In that study, the result is based on the impurity arising from stiffness between lumped mass, yielding $k_r = \arccos(1-\gamma)$, where γ represents the stiffness ratio between the host and the impurity. This result arises from the fundamental principles of mechanical waves, as the related physical quantities (e.g., wave velocity, frequency) are inversely proportional to inertia (mass) and directly dependent on potential (stiffness).

Next, we determine the wave number or frequency of the multiple reflectionless modes in our system by substituting effective mass [Eq. (5)] for the mass quantities (i.e., $\rho \mapsto \rho_{\mathrm{eff}}$). The transmissionless modes can be identified by setting $|T|^2 = 0$, where the divergence of the effective mass results in the emergence of these modes. As a result, we can analytically obtain the slope of the asymmetric line profile, which exhibits a sharp transition from total transmission to reflection. The degree of this slope can be adjusted by tuning the local resonance of the system.

B. Numerical approach

For the numerical simulation, we solve the equations of motion [Eqs. (1) and (2)] directly through a Runge-Kutta method using Matlab's ODE45 routine. To focus exclusively on the transmission efficiency of wave scattering induced by impurities, we consider a long chain to exclude the boundary-induced scattering effects on the chain. We apply a sinusoidal perturbation with small dynamic amplitudes to the left end of the chain, thereby confining wave dynamics to near-linear regimes. Appendix E provides the spatial-temporal velocity profiles from the numerical simulations, along with detailed calculation of the transmission coefficient. In this way, by incrementally increasing the frequency in small steps, we obtain the transmission efficiency for each frequency in the impurity-bearing chains.

C. Experimental approach

Here, we describe the experimental setup and data acquisition process for a single-column woodpile structure with impurities. In Fig. 6, we show a digital image of the experimental setup. The woodpile structure consists of 53 slender cylindrical resonators, configured in two different setups: For single impurity-bearing chains, the structure comprises 52 short-length cylinders (30 mm) and one impurity. For double impurity-bearing chains, there are 51 short-length cylinders and two impurities. Adjacent cylindrical resonators are stacked orthogonally in contact, with all cylinders having an identical radius of 5 mm. Since the radii of all cylinders are identical, the contact stiffness between neighboring cylinders is uniform, as determined by Hertzian contact. The vertically aligned cylinder chain is inherently unstable and prone to buckling under compressive loading. To mitigate this instability, we employ guide rods and soft polyurethane foam to support the single-column chain, as shown in the inset of Fig. 6. In particular, the polyurethane foam used in the setup has a significantly lower stiffness compared to the rigidity of the cylinders and the contact stiffness between them. This

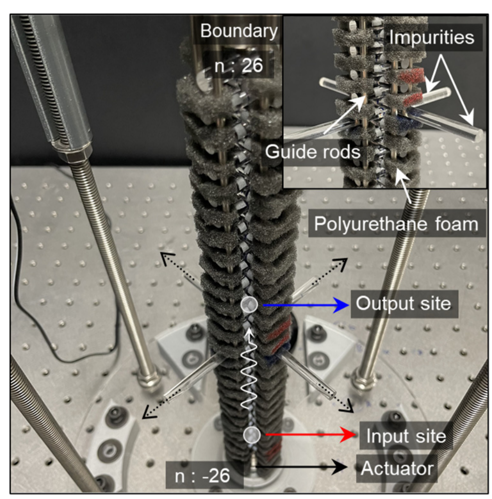

FIG. 6. Experimental setup of the single-column woodpile structure with double impurities. The inset shows a close-up view of the impurity region. Guide rods constrain horizontal motion to ensure structural stability, while soft polyurethane foam suppresses buckling with minimal interference to vertical wave propagation.

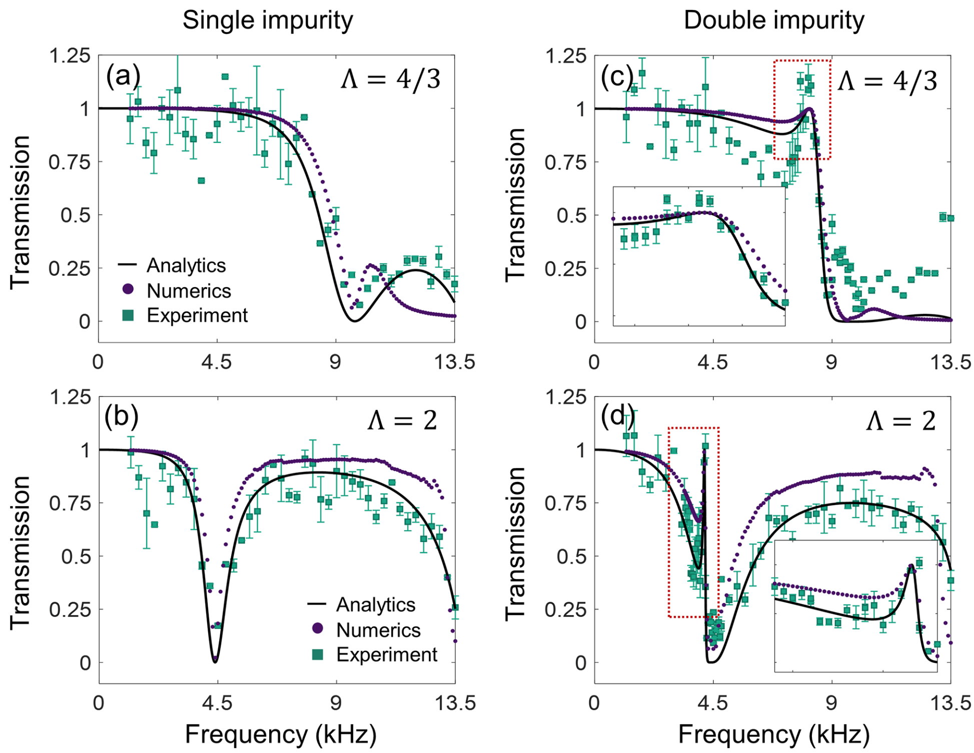

FIG. 7. Transmission of plane waves in a single-column woodpile chain with impurities. The length ratio Λ between the impurity and host cylinders is set to $\Lambda = 4/3$ (top) and $\Lambda = 2$ (bottom). The left panels show the results for a single impurity, while the right panels correspond to a double impurity configuration. The region exhibiting a pronounced resonance effect induced by the double impurity (highlighted with red boxes) is enlarged and presented as an inset.

design minimizes interference with wave propagation in the chain, enabling precise measurements of the wave dynamics.

Under the described configuration, precompression is applied to the chain through a boundary load at the top. This ensures the system operates within the linear regime for wave dynamics. A piezoelectric actuator (Piezomechanik PSt 5001025) positioned at the bottom of the chain drives the first cylinder ($n = -26$). To examine the transmission efficiency across the acoustic band of the host cylinder, harmonic excitations are applied from 1.2 to 13.5 kHz in 300 Hz increments. Additionally, to capture fine details near the RT and Fano resonance frequencies, high-resolution measurements are performed using a 50 Hz step size in those specific regions. The localized out-of-plane vibration (velocity unit) near the contact sites of the cylinders is then measured using a laser Doppler vibrometer. Similar to our numerical approach (see Appendix E), we estimate transmission efficiency by comparing the amplitude of the input site ($n = -3$) and the output site ($n = 3$) near the impurities (n = 0). We note that the numerical and experimental configurations differ because the simulations use a long chain to minimize boundary-induced reflections, whereas the experiments use a shorter chain and near-impurity measurements to reduce accumulated damping and maintain structural stability. These experimental measurements are still subject to significant wave attenuation due to damping effects, including material dissipation, contact friction, and thermal influences. Therefore, we calibrate the experimental results by normalizing them against the measurements obtained from a homogeneous woodpile structure consisting solely of host cylinders. In the homogeneous reference chain, the wave amplitude generally decreases along the propagation direction because of dissipative effects, mainly associated with cylinder-to-cylinder contacts, material damping, and contact friction. For each excitation frequency, this baseline attenuation is quantified from the output-to-input velocity amplitude ratio measured in the homogeneous reference chain and is then used as a reference for the impurity-bearing chain. This procedure allows us to isolate the scattering effect of the impurities and to evaluate the transmission efficiency reliably, even in the presence of various damping effects.

IV. COMPARISON BETWEEN ANALYTICAL, NUMERICAL, AND EXPERIMENTAL RESULTS

We now compare our analytical results with numerical simulations and experimental measurements for two selected cases: length ratios $\Lambda = 4/3$ and $\Lambda = 2$. These two values of Λ are selected to examine how the frequency of the impurity-induced local resonance within the acoustic band of the host cylinder affects wave transmission. Both $\Lambda = 4/3$ and $\Lambda = 2$ fall within the acoustic band of the host cylinder, but their local resonances appear at different frequency regions—higher for $\Lambda = 4/3$ and lower for $\Lambda = 2$—due to the difference in impurity cylinder length. Before discussing the double-impurity cases, we first present the transmission coefficients for a single-impurity chain in Figs. 7(a) and 7(b), where the analytical results are shown as solid lines, the numerical results as circular markers, and the experimental data as square markers. For the case of $\Lambda = 4/3$, the transmission coefficient remains close to unity in the low-frequency regime and gradually decreases as the excitation frequency increases. In contrast, for $\Lambda = 2$, a distinct and sharp dip—corresponding to zero transmission—emerges due to destructive interference between the propagating wave and the low-frequency local resonance mode of the impurity cylinder, which interact in an out-of-phase manner.

We now turn to the double-impurity chain, focusing on the experimental verification of the transition from a mechanical analog of the RT resonance to a Fano resonance, driven by strong coupling with impurity-induced local resonance. In Figs. 7(c) and 7(d), we show the transmission coefficients for the double-impurity cases. For $\Lambda = 4/3$, the overall trend resembles that of the single-impurity chain, exhibiting a gradual decrease in transmission as the excitation frequency increases. However, a notable transmission peak emerges near 8.5 kHz (highlighted by the red box and shown in the inset), where nearly full transmission occurs despite the presence of two impurities. This phenomenon corresponds to a mechanical analog of the RT resonance, as previously reported in Ref. [24], and is consistently observed in our experimental data.

In the $\Lambda = 4/3$ case, the RT resonance and the impurity-induced local resonance are relatively separated in frequency. In contrast, for $\Lambda = 2$, they are expected to lie much closer. This spectral proximity leads to strong interference between the two modes and induces a transition toward a Fano-type resonance, as discussed in Sec. III. As shown in Fig. 7(d), we experimentally observe an asymmetric line shape with a sharp transition between transmission and reflection, which is a characteristic signature of Fano resonance. The corresponding space-time velocity profiles, which visualize the RT-like transmission and local-resonance-induced reflection regimes, are provided in Appendix E These observations are in excellent agreement with both analytical predictions and numerical simulations. Importantly, this transition is achieved simply by adjusting the length of the impurity cylinders, which in turn controls the strength of local resonance coupling. As seen across all the results presented in Fig. 7, there is a slight mismatch in the low-frequency range of the experimental data. This discrepancy is likely due to imperfections in the chain configuration, such as misalignment between cylinders or deviations from centered contact. In addition, small deviations in the numerical results can arise from residual finite-size effects and transient components in the time-domain simulations, whereas damping in the experiment can suppress such parasitic reflections after normalization with the homogeneous reference chain. Nevertheless, the overall trend observed in all experimental results shows good agreement with both the analytical predictions and numerical simulations.

V. MECHANICAL ANALOG OF ELECTROMAGNETICALLY INDUCED TRANSPARENCY

Following this finding, a natural question arises: as the length of the impurity cylinders increases, multiple local resonance modes are expected to emerge within the acoustic band of the host cylinders. How, then, will the transmission behavior be affected by such changes? To address this question, it is essential to emulate the complex wave dynamics associated with these multiple local resonance modes in the continuous impurity cylinders. This is made straightforward by our physics-informed discrete element modeling, specifically because it is rooted in continuum mechanics.

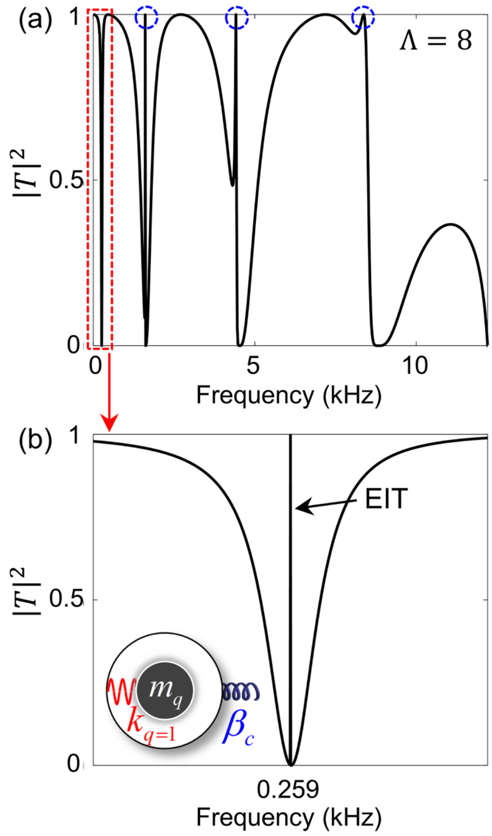

FIG. 8. (a) Transmission coefficients for plane wave scattering in a woodpile chain with double impurities of length ratio $\Lambda = 8$. Four reflectionless modes are identified (blue circles). (b) Enlarged view of the frequency region near the first mode, highlighted by a red box in panel (a), in which a narrow transparency window appears within a broader absorption region.

In Fig. 8, we present the transmission coefficient for the case of $\Lambda = 8$, with particular focus on a double-impurity chain. Two notable features are evident in the results. First, we observe multiple full-transmission peaks originating from RT resonance induced by the presence of double impurity cylinders. Notably, four distinct peaks are identified in this case. As the mode order decreases—that is, toward lower frequency ranges—the fully transmitted peaks and the adjacent transmission dips become increasingly close, resulting in sharply contrasting regions. The second intriguing feature lies in the transmission profile of the first mode (highlighted in the magnified view below). Unlike the typical asymmetric lineshape of a Fano resonance, this peak exhibits a symmetric and sharp feature embedded within an absorption band. The profile closely resembles the characteristic lineshape of EIT [43], in which a narrow transparency window appears within a broader absorption region.

In this regard, it is worth noting that, as the frequency decreases, the fully transmitted RT resonance and the fully reflected local resonance gradually approach each other. This proximity leads to the emergence of an EIT-like lineshape, resulting from the balanced interference between the localized and continuum modes. Such EIT-like phenomena have been actively studied in optics, motivated by their potential to enable slow-wave propagation, narrowband filtering, and tunable wave transmission [37,44]. These studies typically achieved transparency by introducing slight detuning between two nearly identical resonators [45,46]. In contrast, in our system, the two impurities are identical and share the same intrinsic local resonance. Nonetheless, two distinct resonances—the fully transmitted RT resonance and the fully reflected local resonance—arise from different physical mechanisms within the same impurity configuration. The EIT-like behavior observed here results from the slight spectral separation between these resonances, similar to the mechanism exploited in optical systems. However, unlike in optics where the resonances originate from physically distinct resonators, in our system they emerge from different dynamic processes within two identical impurities, resulting in distinct resonance behaviors. This characteristic highlights that all resonance behaviors—including RT resonances, Fano-like resonances, and EIT-like transparency—can be controllably achieved simply by tuning the degree of local resonance coupling.

VI. CONCLUSION

In the present work, we have investigated linear wave scattering in a one-dimensional locally resonant woodpile structure containing single and double impurities, and demonstrated that tuning the strength of local resonance coupling enables the system to exhibit a variety of distinct resonance phenomena. Specifically, a transmission behavior resembling the classical RT resonance—characterized by reflectionless transmission through a double-impurity configuration—evolves into a sharp Fano resonance when the impurity's local resonance mode strongly couples to the propagating wave. Moreover, as the RT resonance and the local resonance become spectrally closer—which can be induced by using longer impurity cylinders—their interference with the continuum gives rise to a symmetric, narrow transparency window, analogous to EIT. These scattering behaviors are consistently observed across analytical modeling, numerical simulations, and experimental measurements, confirming the robustness of the underlying physical mechanisms. The ability to seamlessly tune between RT-like, Fano, and EIT-like responses within a single mechanical platform highlights the versatility of locally resonant woodpile structures. This tunability allows a macroscopic lattice to emulate wave interference effects typically associated with quantum or atomic systems, offering a practical platform for exploring fundamental resonance phenomena. Moreover, such control over wave scattering enables the design of adaptive vibration isolators, tunable filters, and wave-based switches within a single reconfigurable structure.

Looking ahead, several directions for future research can build upon these findings. One key avenue is to explore nonlinear extensions by introducing large-amplitude excitations, which activate Hertzian contact nonlinearity and may give rise to amplitude-dependent analogs of Fano or EIT resonances. Another promising direction is to explore disordered systems rather than merely placing a disordered segment in otherwise homogeneous chains. Such systems may exhibit Anderson localization, and their interplay with local resonance coupling remains largely unexplored.

ACKNOWLEDGMENTS

This work was financially supported by the POSCO-POSTECH-RIST Convergence Research Center program funded by POSCO, and the National Research Foundation (NRF) grant funded by the Ministry of Science and ICT (MSIT) of the Korean government (RS-2024-00356928). E.K. acknowledges support from the NRF Grant No. (RS-2025-24523271) funded by the MSIT the Korean government. Y.J. acknowledges the POSTECH PIURI fellowship.

DATA AVAILABILITY

The data supporting this study's findings are available within the article.

APPENDIX A: HERTZIAN CONTACT

The interaction between adjacent cylindrical beams follows a nonlinear force-displacement relationship described by the Hertzian contact model [39], expressed as $F = A_r\delta^{3/2}$, where F is the contact force and δ is the relative deformation at the contact point. The contact stiffness coefficient A_r is determined by the geometry, material properties, and the contact angle ϕ between neighboring cylinders. For the special case of perpendicular contact ($\phi = 90^\circ$), the coefficient simplifies to $A_r = 2E\sqrt{R_c}/3(1-\nu^2)$, where R_c the radius of the beams, and E and ν denote Young's modulus and Poisson's ratio, respectively. As mentioned in the main text, assuming that dynamic perturbations are small compared to the precompression force F_0, the nonlinear contact behavior can be approximated by an effective linear stiffness. In this regime, the linearized contact stiffness is given by

$$\beta_r = \left.\frac{dF}{d\delta}\right|_{\delta=\delta_0} = \frac{3}{2}A_r^{2/3}F_0^{1/3}, \tag{A1}$$

where δ_0 is the static displacement corresponding to the precompression force F_0.

APPENDIX B: DISCRETIZED EQUIVALENT MASS AND SPRING STIFFNESS

This Appendix provides the equivalent mechanical coefficients used in the discrete element model for various cylinder lengths. The equivalent mechanical parameters are obtained using the physics-informed DEM procedure developed in Ref. [23]. In this procedure, a cylindrical beam in a periodic chain is treated as a continuum unit cell, and its characteristic frequencies are calculated using Timoshenko beam theory with wave-number-dependent boundary conditions at the contact point. Three representative wave states are considered [see Fig. 2(b)]: the in-phase state at $ka = 0$, which gives the onset frequency; the out-of-phase state at $ka = \pi$, which gives the cutoff frequency; and the stationary local-

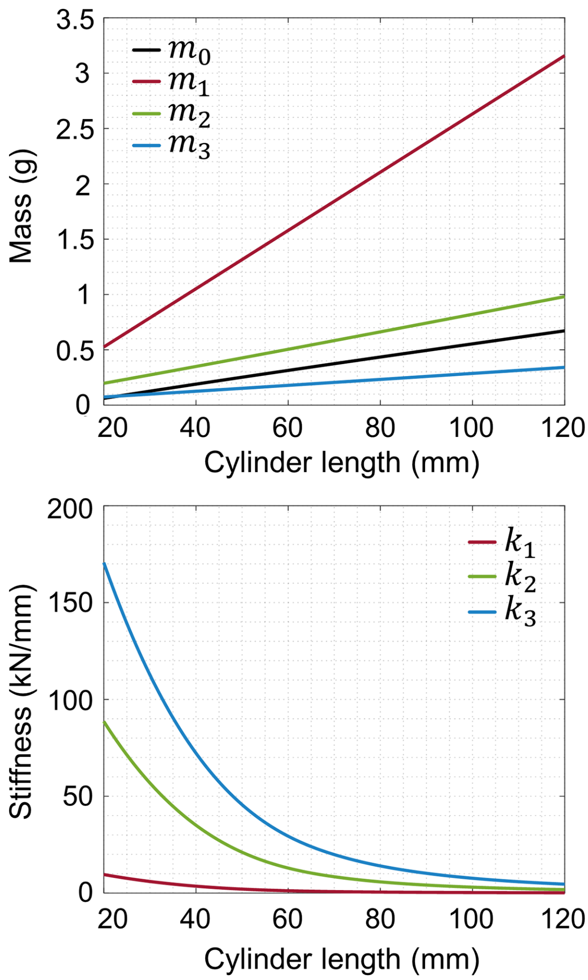

FIG. 9. Equivalent mechanical parameters used in the discrete element model for various cylinder lengths. Among the infinite number of possible modes, only the parameters up to the third local resonance mode are presented.

resonance state at $ka = -\infty i$, which gives the local resonance frequency. These characteristic frequencies are then substituted into the dispersion relation of the mass-with-mass DEM unit cell, and the resulting algebraic equations determine the primary mass m_0, the local resonator masses m_q, and the spring constants k_q. Therefore, the parameters are not obtained by phenomenological fitting, but are determined from continuum beam dynamics and the corresponding wave states of the periodic chain. Since the characteristic bending frequencies depend strongly on the cylinder length, changing the length ratio Λ directly modifies the equivalent DEM parameters.

Following this procedure, Fig. 9 lists the values of the primary mass, local resonator masses, and local stiffnesses for each cylinder length considered [see the unit cell in Fig. 1(c)]. Among the infinite number of possible modes, this Appendix presents only the parameters associated with the first three local resonance modes. We note that the variation in local resonance coupling is achieved solely by adjusting the length of the cylindrical elements. Once again, we refer readers to Ref. [23] for a comprehensive description of the mathematical derivation of the physics-informed discrete element model.

APPENDIX C: LINEAR SYSTEM OF EQUATION FOR DOUBLE IMPURITY

Here, we provide the linear system of equations for the double impurity case,

$$\mathcal{S}\begin{pmatrix} T \\ R \\ T_0 \\ R_0 \end{pmatrix} = \mathcal{D}, \tag{C1}$$

where the matrix $\mathcal{S}$ and the vector $\mathcal{D}$ are defined as follows:

$$\mathcal{S} = \begin{pmatrix} 0 & B_1 & \beta_r e^{-ik_\delta} & \beta_r e^{ik_\delta} \\ 0 & \beta_r e^{2ik} & C_1 & D_1 \\ \beta_r e^{ik} & 0 & C_2 & D_2 \\ A_1 & 0 & \beta_r & \beta_r \end{pmatrix}, \tag{C2}$$

with matrix elements given by

$$A_1 = -\left(2\beta_r - \sum_q k_q\Delta_q - m_0\omega^2\right)e^{ik} + \beta_r e^{2ik}, \tag{C3}$$

$$B_1 = \beta_r e^{3ik} - \left(2\beta_r - \sum_q k_q\Delta_q - m_0\omega^2\right)e^{2ik}, \tag{C4}$$

$$C_1 = \beta_r - \left(2\beta_r - \sum_q \widetilde{k}_q\widetilde{\Delta}_q - \widetilde{m}_0\omega^2\right)e^{-ik_\delta}, \tag{C5}$$

$$C_2 = \beta_r e^{-ik_\delta} - \left(2\beta_r - \sum_q \widetilde{k}_q\widetilde{\Delta}_q - \widetilde{m}_0\omega^2\right), \tag{C6}$$

$$D_1 = \beta_r - \left(2\beta_r - \sum_q \widetilde{k}_q\widetilde{\Delta}_q - \widetilde{m}_0\omega^2\right)e^{ik_\delta}, \tag{C7}$$

$$D_2 = \beta_r e^{ik_\delta} - \left(2\beta_r - \sum_q \widetilde{k}_q\widetilde{\Delta}_q - \widetilde{m}_0\omega^2\right). \tag{C8}$$

The right-hand side vector $\mathcal{D}$ is given by

$$\mathcal{D} = (E_1, \quad -\beta_r e^{-2ik}, \quad 0, \quad 0)^T, \tag{C9}$$

where

$$E_1 = \left(2\beta_r - \sum_q k_q\Delta_q - m_0\omega^2\right)e^{-2ik} - \beta_r e^{-3ik}. \tag{C10}$$

APPENDIX D: TRANSMISSION WITHOUT LOCAL RESONANCE

This Appendix presents the transmission coefficients for plane wave scattering in a double-impurity system in the absence of local resonance. As noted in the main text, the local resonance effect is excluded by taking the local stiffness to the limit of infinity, effectively suppressing internal vibration.

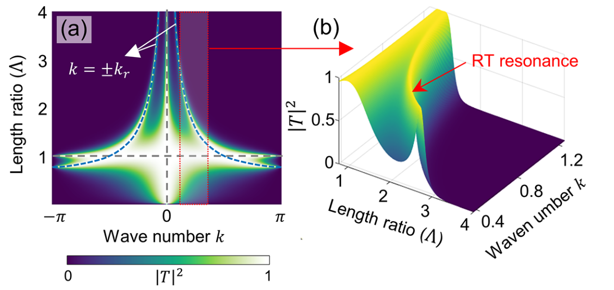

FIG. 10. (a) Transmission coefficients as a function of wave number k and length ratio Λ in a double-impurity system without local resonance. The blue dashed line indicates the analytically derived RT resonance condition corresponding to Eq. (16) in the main text. (b) Enlarged view of the boxed region in panel (a), showing the detailed transmission profile.

Under this condition, the wave dynamics closely resemble those of a classical granular crystal, and as demonstrated in Ref. [24], this setting gives rise to only RT resonance. In Fig. 10(a), we show the transmission coefficient as a function of the wave number k and the length ratio Λ; the blue dashed line indicates the RT resonance mode—i.e., the reflectionless condition ($k = \pm k_r$)—which is analytically obtained from Eq. (16) in the main text. The region highlighted by the red box is enlarged in Fig. 10(b), clearly showing the characteristic profile of the RT resonance. Since no local resonance coupling exists in this system, increasing the length ratio Λ does not lead to additional interference effects, and only the RT resonance mode remains, with its wave number asymptotically approaching zero.

APPENDIX E: NUMERICAL SIMULATIONS

This Appendix provides spatial-temporal velocity profiles from numerical simulations, along with the procedure for quantitatively evaluating transmission efficiency in impurity-bearing chains. In the discrete element model, a sinusoidal perturbation with a specific frequency and very small amplitude is applied at the left end of the chain to ensure that the system response remains within the near-linear regime. In Fig. 11, we show space-time contour plots of velocity for a 241-particle chain with double impurities placed between particles $n = -1$ and $n = 2$, where the length ratio is set to $\Lambda = 2$. Specifically, Fig. 11(a) displays the reflectionless mode (RT resonance), where nearly full wave transmission is observed, with only a phase shift near the impurity region (see inset). In contrast, Fig. 11(b) shows the transmissionless mode, where most of the wave is blocked in front of the impurity due to the vibration isolation effect caused by the out-of-phase motion of the local resonance mode. These two limiting cases provide a direct visualization of the scattering mechanisms underlying the Fano-like response discussed in the main text. The reflectionless mode corresponds to the RT-like resonance, whereas the transmissionless mode originates from impurity-induced local resonance. When these two mechanisms are spectrally close, their superposition produces the sharp transition from nearly full transmission to nearly zero transmission that appears as the Fano-like resonance.

To quantify transmission efficiency, we extract velocity signals at two specific particle locations: $n = -112$ for the incident wave and $n = +8$ for the transmitted wave. These profiles are shown in the bottom panels of Figs. 11(a) and 11(b). The extracted velocity signals contain both transient

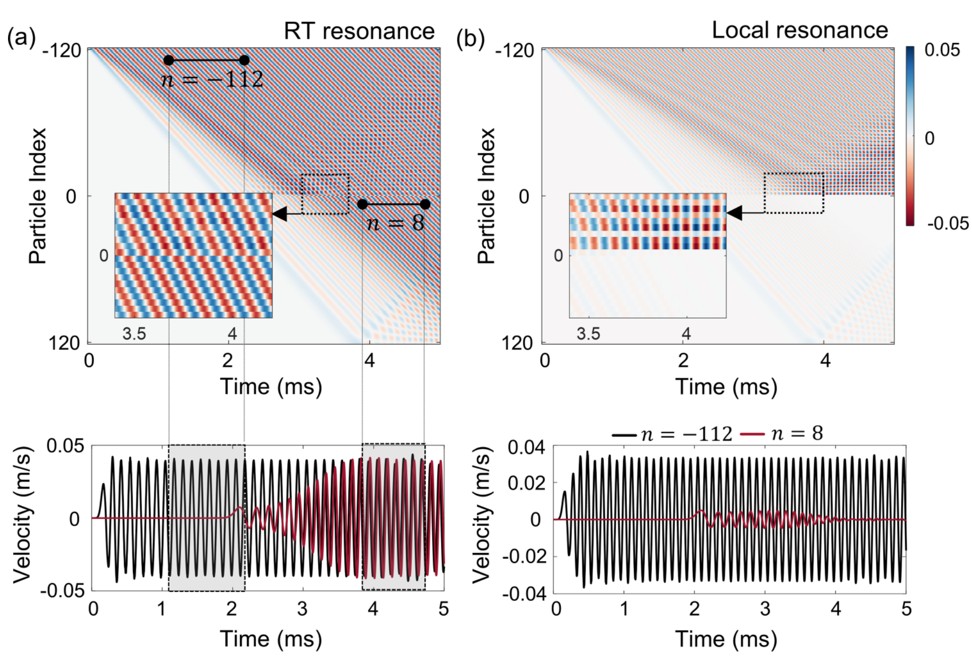

FIG. 11. (a) Space-time contour plot of velocity for the reflectionless mode (RT resonance) in a double-impurity chain. The inset shows a phase shift near the impurities with nearly full transmission. (b) Space-time contour plot for the transmissionless mode with strong local resonance, where the wave is mostly reflected at the impurity location. Bottom panels in (a) and (b) show the velocity profiles at two selected particles($n = -112$ and $n = +8$) used to quantify the transmission efficiency. The black boxes indicate the steady-state time windows used to calculate the transmission efficiency.

and steady-state components. To isolate the steady-state response, we select a time window that appears sufficiently after the initial excitation. This time window is indicated by a black line segment with circular endpoints in Fig. 11(a). Within these steady-state windows (highlighted by black boxes in the bottom panel), we calculate the peak amplitude of the velocity response. The transmission efficiency $\bar{T}$ is then determined as the ratio of the transmitted to incident velocity amplitudes. The transmission efficiency $\bar{T}$, defined in terms of velocity amplitudes, is expected to be equivalent to the displacement-based transmission ratio derived analytically in Sec. III, under the ideal condition of harmonic responses.

[1] V. F. Nesterenko, *Dynamics of Heterogeneous Materials* (Springer, New York, NY, 2001).

[2] M. A. Porter, P. G. Kevrekidis, and C. Daraio, Granular crystals: Nonlinear dynamics meets materials engineering, Phys. Today **68**(11), 44 (2015).

[3] C. Chong, M. A. Porter, P. G. Kevrekidis, and C. Daraio, Nonlinear coherent structures in granular crystals, J. Phys.: Condens. Matter **29**, 413003 (2017).

[4] S. Sen, J. Hong, J. Bang, E. Avalos, and R. Doney, Solitary waves in the granular chain, Phys. Rep. **462**, 21 (2008).

[5] P. G. Kevrekidis, Non-linear waves in lattices: Past, present, future, IMA J. Appl. Math. **76**, 389 (2011).

[6] G. Theocharis, N. Boechler, and C. Daraio, Nonlinear periodic phononic structures and granular crystals, in *Acoustic Metamaterials and Phononic Crystals* (Springer, Berlin, Heidelberg, 2012), pp. 217–251.

[7] M. Meidani, E. Kim, F. Li, J. Yang, and D. Ngo, Tunable evolutions of wave modes and bandgaps in quasi-1D cylindrical phononic crystals, J. Sound Vib. **334**, 270 (2015).

[8] R. Chaunsali, E. Kim, A. Thakkar, P. Kevrekidis, and J. Yang, Demonstrating an *in situ* topological band transition in cylindrical granular chains, Phys. Rev. Lett. **119**, 024301 (2017).

[9] J. Hong, Universal power-law decay of the impulse energy in granular protectors, Phys. Rev. Lett. **94**, 108001 (2005).

[10] R. Chaunsali, M. Toles, J. Yang, and E. Kim, Extreme control of impulse transmission by cylinder-based nonlinear phononic crystals, J. Mech. Phys. Solids **107**, 21 (2017).

[11] Y. Jang, E. Kim, J. Yang, and J. Rho, Sculpt wave propagation in 3D woodpile architecture through vibrational mode coupling, Mech. Syst. Sig. Process. **224**, 112112 (2025).

[12] N. Boechler, G. Theocharis, and C. Daraio, Bifurcation-based acoustic switching and rectification, Nat. Mater. **10**, 665 (2011).

[13] E. Kim, R. Chaunsali, and J. Yang, Gradient-index granular crystals: From boomerang motion to asymmetric transmission of waves, Phys. Rev. Lett. **123**, 214301 (2019).

[14] F. Li, P. Anzel, J. Yang, P. G. Kevrekidis, and C. Daraio, Granular acoustic switches and logic elements, Nat. Commun. **5**, 5311 (2014).

[15] J. Yang, C. Silvestro, S. N. Sangiorgio, S. L. Borkowski, E. Ebramzadeh, L. D. Nardo, and C. Daraio, Nondestructive evaluation of orthopaedic implant stability in THA using highly nonlinear solitary waves, Smart Mater. Struct. **21**, 012002 (2012).

[16] E. Kim and J. Yang, Wave propagation in single column woodpile phononic crystals: Formation of tunable band gaps, J. Mech. Phys. Solids **71**, 33 (2014).

[17] E. Kim, F. Li, C. Chong, G. Theocharis, J. Yang, and P. Kevrekidis, Highly nonlinear wave propagation in elastic woodpile periodic structures, Phys. Rev. Lett. **114**, 118002 (2015).

[18] E. Kim, J. Yang, H. Hwang, and C. W. Shul, Impact and blast mitigation using locally resonant woodpile metamaterials, Int. J. Impact Eng. **101**, 24 (2017).

[19] Y. Jang, B. Oh, E. Kim, and J. Rho, Bidirectional asymmetric frequency conversion in nonlinear phononic crystals, Phys. Rev. Lett. **135**, 036603 (2025).

[20] Y. Jang, S. Kim, M. Kim, G. Kim, E. Kim, and J. Rho, Mode-coupled infinite topological edge state in bulk-lattice-merged mechanical Su-Schrieffer-Heeger chain, Extreme Mech. Lett. **77**, 102334 (2025).

[21] Y. Jang, S. Kim, E. Kim, and J. Rho, Singular topological edge states in locally resonant metamaterials, Sci. Bull. **70**, 1080 (2025).

[22] Y. Jang, S. Kim, D. Lee, E. Kim, and J. Rho, Bound states to bands in the continuum in cylindrical granular crystals, Phys. Rev. Lett. **134**, 136901 (2025).

[23] Y. Jang, E. Kim, J. Yang, and J. Rho, Physics-informed discrete element modeling for the bandgap engineering of cylinder chains, Appl. Math. Modell. **125**, 571 (2024).

[24] A. J. Martínez, H. Yasuda, E. Kim, P. G. Kevrekidis, M. A. Porter, and J. Yang, Scattering of waves by impurities in precompressed granular chains, Phys. Rev. E **93**, 052224 (2016).

[25] J. J. Sakurai and J. Napolitano, *Modern Quantum Mechanics* (Cambridge University Press, Cambridge, UK, 2020).

[26] L. Novotny, Strong coupling, energy splitting, and level crossings: A classical perspective, Am. J. Phys. **78**, 1199 (2010).

[27] C. L. Garrido Alzar, M. A. G. Martinez, and P. Nussenzveig, Classical analog of electromagnetically induced transparency, Am. J. Phys. **70**, 37 (2002).

[28] W. Frank and P. von Brentano, Classical analogy to quantum mechanical level repulsion, Am. J. Phys. **62**, 706 (1994).

[29] H. J. Maris and Q. Xiong, Adiabatic and nonadiabatic processes in classical and quantum mechanics, Am. J. Phys. **56**, 1114 (1988).

[30] M. Hasan, Y. Starosvetsky, A. Vakakis, and L. Manevitch, Nonlinear targeted energy transfer and macroscopic analog of the quantum Landau-Zener effect in coupled granular chains, Physica D **252**, 46 (2013).

[31] C. Wang, A. Kanj, A. Mojahed, S. Tawfick, and A. F. Vakakis, Experimental Landau-Zener tunneling for wave redirection in nonlinear waveguides, Phys. Rev. Appl. **14**, 034053 (2020).

[32] A. J. Martínez, P. G. Kevrekidis, and M. A. Porter, Superdiffusive transport and energy localization in disordered granular crystals, Phys. Rev. E **93**, 022902 (2016).

[33] E. Kim, A. J. Martínez, S. E. Phenisee, P. G. Kevrekidis, M. A. Porter, and J. Yang, Direct measurement of superdiffusive energy transport in disordered granular chains, Nat. Commun. **9**, 640 (2018).

[34] S. D. Huber, Topological mechanics, Nat. Phys. **12**, 621 (2016).
[35] H. Nassar, B. Yousefzadeh, R. Fleury, M. Ruzzene, A. Alù, C. Daraio, A. N. Norris, G. Huang, and M. R. Haberman, Nonreciprocity in acoustic and elastic materials, Nat. Rev. Mater. **5**, 667 (2020).
[36] J. D. Maynard, Acoustical analogs of condensed-matter problems, Rev. Mod. Phys. **73**, 401 (2001).
[37] A. E. Miroshnichenko, S. Flach, and Y. S. Kivshar, Fano resonances in nanoscale structures, Rev. Mod. Phys. **82**, 2257 (2010).
[38] S. E. Harris, Electromagnetically induced transparency, Phys. Today **50**(7), 36 (1997).
[39] K. L. Johnson and K. L. Johnson, *Contact Mechanics* (Cambridge University Press, Cambridge, UK, 1987).
[40] L. Brillouin, *Wave Propagation in Periodic Structures: Electric Filters and Crystal Lattices*, 2nd ed. (Dover Publications, New York, NY, 1953), originally published in 1946 by McGraw-Hill.
[41] D. J. Inman and R. C. Singh, *Engineering Vibration* (Prentice Hall, Englewood Cliffs, NJ, 1994), Vol. 3.
[42] H. Yasuda, E. G. Charalampidis, P. K. Purohit, P. G. Kevrekidis, and J. R. Raney, Wave manipulation using a bistable chain with reversible impurities, Phys. Rev. E **104**, 054209 (2021).
[43] M. Fleischhauer, A. Imamoglu, and J. P. Marangos, Electromagnetically induced transparency: Optics in coherent media, Rev. Mod. Phys. **77**, 633 (2005).
[44] M. F. Limonov, M. V. Rybin, A. N. Poddubny, and Y. S. Kivshar, Fano resonances in photonics, Nat. Photonics **11**, 543 (2017).
[45] D. D. Smith, H. Chang, K. A. Fuller, A. T. Rosenberger, and R. W. Boyd, Coupled-resonator-induced transparency, Phys. Rev. A **69**, 063804 (2004).
[46] M. F. Yanik, W. Suh, Z. Wang, and S. Fan, Stopping light in a waveguide with an all-optical analog of electromagnetically induced transparency, Phys. Rev. Lett. **93**, 233903 (2004).